



## Evaluation of correlated Pandora column observations and *in situ* surface air quality measurements during GMAP campaign

Lim-Seok Chang<sup>1</sup>, Donghee Kim<sup>1</sup>, Hyunkee Hong<sup>1</sup>, Deok-Rae Kim<sup>1</sup>, Jeonga Yu<sup>1</sup>,  
Kwangyul Lee<sup>1</sup>, Hanlim Lee<sup>2</sup>, Daewon Kim<sup>2</sup>, Jinkyu Hong<sup>3</sup>, Hyun-Young Jo<sup>4</sup>,  
and Cheol-Hee Kim<sup>4,5</sup>

<sup>1</sup> *Environmental Satellite Center, National Institute of Environmental Research, Incheon, 22689, Republic of Korea*

<sup>2</sup> *Department of Spatial Information Engineering, Pukyong National University, Busan, 48547, Republic of Korea*

<sup>3</sup> *Department of Atmospheric Sciences, Yonsei University, Seoul, 03722, Republic of Korea*

<sup>4</sup> *Institute of Environmental Studies, Pusan National University, Busan, 46241, Republic of Korea*

<sup>5</sup> *Department of Atmospheric Sciences, Pusan National University, Busan, 46241, Republic of Korea*

---

### Correspondence:

Cheol-Hee Kim (chkim2@pusan.ac.kr), and Lim-Seok Chang (lschang@korea.kr)



1   **Abstract.**

2   To validate the Geostationary Environment Monitoring Spectrometer (GEMS), the GEMS  
3   Map of Air Pollution (GMAP) campaign was conducted during 2020–2021 by integrating  
4   Pandora Asia Network, aircraft, and *in situ* measurements. In the present study, GMAP-2020  
5   measurements were applied to evaluate urban air quality and explore the synergy of Pandora  
6   column (PC) NO<sub>2</sub> measurements and surface *in situ* (SI) NO<sub>2</sub> measurements for Seosan, South  
7   Korea, where large point source (LPS) emissions are densely clustered. Due to the difficulty  
8   of interpreting the effects of LPS emissions on air quality downwind of Seosan using SI  
9   monitoring networks alone, we used a combination of PC and SI measurements, and explored  
10   the synergy of this approach through correlation analysis of PC-NO<sub>2</sub> and SI-NO<sub>2</sub>.  
11   Agglomerative hierarchical clustering using vertical meteorological variables combined with  
12   PC-NO<sub>2</sub> and SI-NO<sub>2</sub> yielded three distinct conditions: synoptic wind-dominant (SD), mixed  
13   (MD), and local wind-dominant (LD). These results suggested meteorology-dependent  
14   correlations between PC-NO<sub>2</sub> and SI-NO<sub>2</sub>. Overall, yearly daytime mean (11:00–17:00 KST)  
15   PC-NO<sub>2</sub> and SI-NO<sub>2</sub> statistical data showed good linear correlations ( $R = \sim 0.73$ ); however,  
16   these correlations were dependent on meteorological conditions. SD conditions characterized  
17   by higher wind speeds and planetary boundary layer heights suppressed fluctuations in both  
18   PC-NO<sub>2</sub> and SI-NO<sub>2</sub>, driving a uniform vertical NO<sub>2</sub> structure with higher correlations,  
19   whereas under LD conditions, stack plumes decoupled from LPS or were transported from  
20   nearby cities, weakening correlations through anomalous vertical NO<sub>2</sub> gradients. However,  
21   under MD conditions, both pollution ventilation due to high surface wind speeds and daytime  
22   photochemical NO<sub>2</sub> loss contributed to stronger correlations through a decline in both PC-NO<sub>2</sub>  
23   and SI-NO<sub>2</sub> toward noon. Thus, Pandora Asia Network observations collected over 13 Asian  
24   countries since 2021 can be utilized for investigation of the vertical complexity of air quality  
25   in combination with SI measurements. The results of this study also indicate that caution is  
26   required when performing GEMS validation using either PC or SI observations alone,  
27   particularly under prevailing local wind meteorological conditions or transport processes.

28

29   **1. Introduction**

30   Rapid developments in environmental remote sensing have led to a new era of air quality  
31   observations, and recent hyperspectral data retrieval technologies have allowed for routine and



accurate monitoring of air pollutants at high spatial and temporal resolution. In particular, the Geostationary Environment Monitoring Spectrometer (GEMS), which was launched on February 18, 2020, measures the total and tropospheric air pollutant columns hourly at spatial resolutions of  $7 \text{ km} \times 8 \text{ km}$  for gas and  $3.5 \text{ km} \times 8 \text{ km}$  for aerosols (Kim and Kim, 2020), facilitating the tracking of pollution transport from local to synoptic scales.

Recent studies have revealed the potential of satellite observations to evaluate surface air quality, particularly in regions with sparse air quality monitoring networks. The main approach is to convert column amounts to surface concentrations using a shape factor of the ratio of the partial column ( $\Omega_{z_0}$ ) within the lowest layer ( $z_0$ ) to the total column ( $\Omega_{\text{total}}$ ), as follows:

$$S = \frac{\Omega_{z_0}}{\Omega_{\text{total}}} \times \frac{C}{\Delta z}$$

where  $S$ ,  $C$  and  $\Delta z$  are the surface concentration, column amount, and thickness of the lowest layer, respectively. Because the shape factor is spatially and temporally variable, it is obtained through the simulation of chemical transport model or aircraft *in situ* measurements. Acquiring accurate profile shape information is critical for determining the close relationship between the column amount and surface concentration. Lamsal et al. (2010) obtained a good correlation between *in situ* surface  $\text{NO}_2$  and Ozone Monitoring Instrument (OMI)-derived surface  $\text{NO}_2$  by applying local shape factors from the GEOS-Chem model, because the vertical  $\text{NO}_2$  profile calculated by GEOS-Chem is consistent with *in situ* aircraft measurements. Other studies have instead assumed a uniform vertical profile to convert column amounts to surface concentrations. Wang and Christopher (2003) found a linear relationship between Moderate Resolution Imaging Spectroradiometer (MODIS) aerosol optical depth (AOD) and surface fine particulate matter ( $\text{PM}_{2.5}$ ) in Alabama, USA, with a high correlation coefficient ( $R$ ) of 0.7. This strong correlation can be explained by a generally uniform planetary boundary layer height (PBLH), as well as by aerosol type and abundance, which is also the case for trace gases.



56 A uniform vertical PBL profile has also been used to successfully scale up surface NO<sub>2</sub> to  
57 column NO<sub>2</sub> in Israeli cities, producing results consistent with the OMI column NO<sub>2</sub> (Boersma  
58 et al., 2009).

59 By contrast, the implications of weak vertical profile correlations remain unclear. Engel-  
60 Cox et al. (2004) found a negative correlation of AOD and surface PM<sub>2.5</sub> in northwestern USA,  
61 and explained it based on elevated haze decoupled from the surface. Thompson et al. (2019)  
62 examined weak correlations between Pandora column (PC) measurements and surface *in situ*  
63 (SI) observations of NO<sub>2</sub> over the Yellow Sea during the Korea–US air quality (KORUS-AQ)  
64 field study, and found that they originated from plumes in China and Seoul hundreds of meters  
65 above the ground (detached from the surface layer). The estimated surface PM<sub>2.5</sub> concentration  
66 was weakly correlated ( $R = 0.4\text{--}0.49$ ) with observed PM<sub>2.5</sub> concentrations in Seoul, because  
67 only PBLH was added to the multi-linear regression model to correlate AOD to surface PM<sub>2.5</sub>  
68 (Kim et al., 2021). This effect may be related to the significant impact of long-range transport  
69 on PM<sub>2.5</sub>, with a contribution of up to 39% in Seoul (Lee et al, 2021). Thus, the wide variability  
70 in the degree of correlation between PC-PM and SI-PM is closely related to vertical profile  
71 variability (Flynn et al., 2016).

72 It appears highly probable that several factors are responsible for the correlations between  
73 PC-NO<sub>2</sub> and SI-NO<sub>2</sub>; therefore, it is necessary to improve our understanding of the degree of  
74 correlation through detailed measurements, including column concentration. In this study, we  
75 focused on the impact of meteorology and chemistry on correlation variability using PC, SI  
76 and aircraft measurements, as well as meteorological observations. Understanding vertical  
77 profile variability is also useful for evaluating the effects of various emissions on urban air  
78 quality, particularly in areas neighboring active large point source (LPS) emission sites.  
79 Quantifying the impact of LPS emissions on downwind cities remains challenging due to the  
80 lack of three-dimensional (3D) measurements. Accurate vertical profile data are also useful for



81 improving remote sensing retrieval algorithms, because the profile shape contributes to the  
82 conversion of slant column density into vertical column density as part of the air mass factor.

83 In mid-2019, the Pandonia Global Network (PGN; <https://pandonia-global-network.org>)  
84 was launched, with support from the National Aeronautics and Space Administration (NASA)  
85 and European Space Agency (ESA), to facilitate the validation and verification of low-orbit  
86 geostationary environmental satellites. This network is attempting to expand air quality  
87 monitoring through integration with existing long-term air quality monitoring stations. Since  
88 2020, the National Institute of Environmental Research, Economic and Social Commission for  
89 Asia and the Pacific, and Korea Environment Corporation have been extending the Pandora  
90 Asia Network to include 13 Asian countries, with support from the Korea International  
91 Cooperation Agency. The Pandora Asia Network is expected to be widely used to study urban  
92 air quality in Asia, which is increasingly deteriorating due to rapid economic growth.

93 As part of the GEMS Map of Air Pollution (GMAP) campaign, a suite of Pandora  
94 instruments was deployed in Seosan, a coastal city of South Korea, from November 2020 to  
95 January 2021 (GMAP-2020), and in the Seoul metropolitan area from October 2021 to  
96 November 2021 (GMAP-2021). In this study, we applied GMAP-2020 measurements to  
97 explore the synergy of PC observations when evaluating air quality over Seosan. Further results  
98 from this research project are also reported in this special issue, including GEMS validation  
99 and urban air quality evaluations based on Pandora, aircraft, surface flux, and *in situ* surface  
100 chemical measurements conducted during GMAP-2020 and GMAP-2021.

101

## 102 **2. GMAP campaign**

103 GEMS was launched on February 19, 2020; it is the first instrument to observe air quality from  
104 a geostationary Earth orbit. GEMS provides hourly air quality data on aerosols and gases at a  
105 spatial resolution of  $7\text{ km} \times 8\text{ km}$ . GEMS is a scanning ultraviolet (UV)–visible spectrometer



106 that observes key atmospheric constituents including O<sub>3</sub>, NO<sub>2</sub>, CO, SO<sub>2</sub>, CH<sub>2</sub>O, CHOCHO,  
107 aerosols, clouds, and UV indices. This mission heralded a new era of satellite air quality  
108 monitoring and will be joined by NASA's Tropospheric Emissions: Monitoring of Pollution  
109 (TEMPO) and ESA's Sentinel-4 to form the GEO Air Quality Constellation in ~3 years, to  
110 cover the most polluted region in the Northern Hemisphere.

111 During GMAP-2020, Pandora instruments were deployed near LPSs in Seosan. Aircraft  
112 measurements and *in situ* surface air quality monitoring systems were used to validate GEMS  
113 and diagnose LPSs located in industrial areas surrounding Seosan. During GMAP-2021,  
114 differential optical absorption spectroscopy (DOAS), car DOAS (Car-DOAS), aircraft, and  
115 Geo-CAPE airborne simulator (GCAS) measurements were also used to validate and evaluate  
116 air quality over the Seoul metropolitan area. In this study, we explored the synergy of Pandora  
117 observations and *in situ* surface measurements, based on measurements collected during  
118 GMAP-2020, by evaluating air quality in industrial Seosan (where LPSs are densely clustered).  
119 During GMAP-2021, multi-perspective observations were obtained from the ground, air, and  
120 space; participating remote sensing instruments were expanded to include multi-axis (Max)  
121 DOAS, Car-DOAS, GCAS, and Pandora data. The target area was the Seoul metropolitan area  
122 and target pollutants included O<sub>3</sub>, HCHO, SO<sub>2</sub>, aerosols, and NO<sub>2</sub>. We investigated the impacts  
123 of vertical profile and sub-pixel variability for trace gases and aerosols, for further GEMS  
124 validation. All measurement sites for both GMAP campaigns are indicated in Figure 1.

125

### 126 3. Methods

#### 127 3.1 Study area

128 Seosan, the target area of the GMAP-2020 campaign, is a small city with a population of  
129 174,780 in 2017; it is accessed via three expressways to the east and four national highways  
130 cross the city. Seosan is located in midwestern South Korea, and is affected by > 300 emission



point sources including LPSs. Coal-fired power plants including Taean, Dangjin, the Hyundai Dangjin steelworks, and the Daesan petrochemistry industrial complex (LPS<sub>1</sub>–LPS<sub>4</sub>, respectively, in Fig. 1) have the highest emission rates in South Korea. The Hyundai Dangjin steelworks (LPS<sub>3</sub>) and Taean and Dangjin power plants (LPS<sub>1</sub> and LPS<sub>2</sub>) emit 10.5, 11, and 8.8 Gg of NO<sub>x</sub> per year, respectively. Although Seosan accounts for only 1.8% of the population of Seoul, its NO<sub>x</sub> emissions (10.2 Gg year<sup>-1</sup>) account for 13.2% of its total NO<sub>x</sub> emissions. The transportation sector of Seosan is a far greater NO<sub>x</sub> source than the industrial sector of Seoul (ratio of 99:1); however, within Seosan, the industrial sector is on par with the transport sector (52:48; <http://airemiss.nier.go.kr>).

During the past decade, the annual mean NO<sub>2</sub> level in Seosan has been 17 ppb, which is approximately half of that in Seoul (31.2 ppb). NO<sub>2</sub> exhibits strong seasonal variation, reaching a minimum in summer and maximum in winter, due to meteorological factors and greater energy use during winter (Kim and Kim, 2020). Therefore, the timing of the GMAP-2020 campaign was well suited to tracking pollution.

### 3.2 Pandora measurements

Pandora measures the UV and visible wavelengths (280–525 nm) of direct sunlight with a spectral resolution of 0.6 nm, to determine the vertical column density of NO<sub>2</sub>, O<sub>3</sub>, and HCHO (Herman et al., 2009). For measurements in Dobson units (DU; 1 DU = 26.9 Pmol cm<sup>-2</sup>), column NO<sub>2</sub> has a very high signal-to-noise ratio (700:1) and very high precision (0.01 DU) for clear skies (Herman et al., 2009). The vertical column density of NO<sub>2</sub> can be determined using DOAS software (Van Roozendaal and Fayt, 2001). Pandora direct-sun measurements are advantageous in that the air mass factor is simplified, and is therefore dependent only on the geography for a known solar zenith angle.

Four Pandora instruments were installed at sites to the south of LPSs (Fig. 1) during the



156 GMAP-2020 campaign, i.e., at Seosan Daehoji, Seosan Dongmun, Seosan City Council, and  
157 Seosan Super Site (PA<sub>1</sub>–PA<sub>4</sub> in Fig. 1). The presence of clouds reduces vertical column density  
158 precision by decreasing the number of photons arriving at Pandora instruments within a fixed  
159 integration time. Therefore, the retrieved Pandora measurements were cloud-screened using an  
160 observed cloud cover of 0.6. Cloud cover was provided by the Korea Meteorological  
161 Administration (KMA), and the precision improvement afforded by cloud screening was  
162 verified by comparing each Pandora-derived vertical column density with the median vertical  
163 column density, with and without cloud screening within the inter-comparison period.

164 At PA<sub>4</sub>, the operating period was extended to cover almost the entire year (November 12,  
165 2020–October 30, 2021) including the GMAP-2020 campaign period, and the Pandora spectra  
166 were processed into vertical column density data for trace gases using the standard NO<sub>2</sub>  
167 algorithm in BlickP software provided by PGN (Cede, 2019). The resultant PC-NO<sub>2</sub> data were  
168 obtained from the PGN website (<https://pandonia-global-network.org>) for the 1-year period  
169 from Nov. 12, 2020 to Oct. 30, 2021, and used as PC-NO<sub>2</sub> statistics.

170

### 171 3.3 Surface and airborne chemical measurements

172 Hourly average data for SI-NO<sub>2</sub> over a period of 1 year were obtained from Ministry of  
173 Environment AQM network stations in Seosan: Pandori, Leewon, Taeon, Dongmoon,  
174 Seongyeon, and Daesan (AQM<sub>1</sub>–AQM<sub>6</sub>, respectively, in Fig. 1). The Seosan Super Site  
175 (PA<sub>4</sub>/AQM<sub>1</sub>) provided hourly data for NO and NO<sub>y</sub> via an NO-DIF-NO<sub>y</sub> analyzer (42i-Y;  
176 Thermo Scientific, Waltham, MA, USA), and for PM<sub>2.5</sub> chemical species using an ambient ion  
177 monitor (AIM; URG 9000D, URG Corp., Chapel Hill, NC, USA). Weekly zero and span  
178 checks were conducted for NO<sub>y</sub> calibration, to ensure that differences between checks  
179 remained < 3%. Water-soluble ions in aerosol and gaseous species were measured hourly using  
180 an AIM, and ion mass balance was used to ensure data quality under the quality control





181 procedures of the AQM network installation and operation guidelines (NIER-GP2021-002).  
182 Aircraft measurements were conducted during the GMAP-2020 and GMAP-2021  
183 campaign periods. During GMAP-2020, nine flights were conducted on 8 days (Nov. 26, 27,  
184 and 28 and Dec. 1, 6, 8, 9, and 12, 2020). The horizontal and vertical distributions of NO<sub>2</sub> and  
185 O<sub>3</sub> over Seosan were measured during GMAP-2020 using an NO<sub>2</sub> monitor (T500U; Teledyne,  
186 Thousand Oaks, CA, USA) and an O<sub>3</sub> analyzer (TEI49C; Thermo Scientific) onboard the  
187 Cessna Grand Caravan 208 B. These instruments had response times of < 40 and < 20 s, and  
188 detection limits of 40 ppt and 1 ppb, respectively. The flight paths included a raster mode over  
189 all of Seosan at a height of 500–700 m and a profiling mode from 500 m to 1.5 km over PA<sub>1</sub>  
190 and PA<sub>4</sub> (Fig. 2).

191

### 192 **3.4 Meteorological measurements**

193 Ground-based hourly observation data for meteorological variables were obtained from Seosan  
194 Automated Synoptic Observing System (ASOS) stations maintained by the KMA, and wind  
195 and temperature profile data were obtained twice daily (0000 and 1200 UTC) via a rawinsonde  
196 instrument at the Osan World Meteorological Organization upper air measurement station  
197 (47122) near Seosan. Due to time constraints of the sonde measurements, information on PBLH  
198 variation was obtained from Unified Model (UM) simulation results provided on the KMA  
199 website (<https://afso.kma.go.kr>).

200 During the GMAP-2020 campaign, a 3D sonic anemometer (CPEC200; Campbell  
201 Scientific Inc., Logan, UT, USA) was also installed on the rooftop at PA<sub>4</sub> for turbulent flux  
202 measurements at the city–atmosphere interface (Hong et al., 2019). All wind components and  
203 sonic temperatures were measured at a 10-Hz sampling rate, and ground-level sensitive heat  
204 flux was measured directly using a 30-min averaging period. Quality controls such as double  
205 rotation, spike removal, and outlier filtering were also applied.



206

### 207 **3.5 Correlation analyses**

208 The purpose of this study was to examine the synergy of PC and SI data obtained during the  
209 GMAP-2020 campaign, and to combine these measurement data to evaluate air quality in  
210 Seosan, South Korea. We attempted to interpret the meteorological and photochemistry data  
211 measured during GMAP-2020, and to demonstrate that caution is required when attempting to  
212 validate GEMS satellite data through comparison with surface observations only, especially in  
213 industrial areas.

214 First, we examined the combined use of year-long PC-NO<sub>2</sub> and SI-NO<sub>2</sub> measurements,  
215 and investigated the factors modulating their correlation. We hypothesized that their  
216 differences were due to meteorological conditions, and performed k-means and agglomerative  
217 hierarchical cluster analyses of meteorological variables using XLSTAT software (Addinsoft  
218 Co., Paris, France). We included eight meteorological variables representing local and synoptic  
219 circulations in the cluster analysis: surface wind speed (Wsfc), 925-hPa temperature (T925),  
220 sea level pressure (Psfc), pressure tendency (dPsfc/dt), 850-hPa wind speed (W850) and its  
221 north–south and east–west components (NS850 and EW850), and 500-hPa geopotential height  
222 (GPH500). We subtracted 30-day moving averages from all data to account for typical seasonal  
223 variation. Monthly averages were used for PC-NO<sub>2</sub> analysis due to the limited availability of  
224 hourly data.

225 Correlations between PC-NO<sub>2</sub> and SI-NO<sub>2</sub> were analyzed in each meteorological group  
226 and the impact of photochemistry was interpreted based on case-specific features. We also  
227 investigated correlations in association with near-surface micrometeorological variables such  
228 as PBLH in each meteorological group.

229

## 230 **4. Results and Discussion**



231

#### 232 **4.1 Correlation analysis results for PC-NO<sub>2</sub> and SI-NO<sub>2</sub>**

233 The yearly PC-NO<sub>2</sub> statistics at four Pandora sites (PA<sub>1</sub>–PA<sub>4</sub>) are summarized in Table 1. The  
234 total averaged PC-NO<sub>2</sub> over all sites was 0.45 DU during GMAP-2020, which is well above  
235 the typical values (0.1–0.2 DU) for Anmyeondo (location is denoted in Figure 1), a  
236 representative background site (Herman et al., 2018). Although site PA<sub>3</sub> is located in a rural  
237 area, it nevertheless exhibited the highest PC-NO<sub>2</sub> amounts, suggesting that plumes were  
238 frequently transported from nearby point sources and/or urban areas.

239 Scatter diagrams of hourly PC-NO<sub>2</sub> and SI-NO<sub>2</sub> measurements from Pandora sites PA<sub>1</sub>–  
240 PA<sub>3</sub> (GMAP-2020) and PA<sub>4</sub> (yearly measurement; November 12, 2020–October 30, 2021) are  
241 shown in Fig. 3a. These hourly data exhibited a fair logarithmic relationship ( $R = 0.45$ ), and a  
242 relatively lower 1:1 linear relationship ( $R = 0.41$ ), where the linear relationship with PC-NO<sub>2</sub>  
243 weakened as SI-NO<sub>2</sub> levels increased. It appears that the SI-NO<sub>2</sub> has a distinct diurnal change  
244 despite the same PC-NO<sub>2</sub>, and higher variable surface NO<sub>2</sub> levels may attribute to relatively  
245 lower linear relationship between PC-NO<sub>2</sub> and SI-NO<sub>2</sub>. To explore these anti-correlation cases  
246 further, we selected the lower and upper bounds of the tendencies; these are plotted in Fig. 3b,  
247 which shows that PC-NO<sub>2</sub> was positively correlated with SI-NO<sub>2</sub> on February 24, 2021 ( $R =$   
248  $0.88$ ), while a negative correlation occurred on April 21, 2021 ( $R = -0.88$ ); thus, there was a  
249 wide range of case-specific correlations.

250 Generally, in remote and clean regions such as the Pacific Ocean, local NO<sub>2</sub>  
251 concentrations are considered to be at background level, and can be used to represent  
252 stratospheric NO<sub>2</sub> amounts. The background level in our study would ideally correspond to the  
253 intercept of the regression model in the PC-SI NO<sub>2</sub> scatter diagram (Fig. 3a). In our analysis of  
254 yearly measurements, the intercept of 0.09 DU was consistent with stratospheric NO<sub>2</sub> amounts  
255 ( $0.10 \pm 0.02$  DU) estimated from the tropospheric monitoring instrument (TROPOMI) at a



256 nadir pass time of approximately at 1330.

257

## 258 **4.2 Impacts of meteorological conditions on correlations between PC-NO<sub>2</sub> and SI-NO<sub>2</sub>**

259 Our k-means cluster analysis distinguished three groups with the lowest within-group variance  
 260 and largest among-group variance. Among the total of 141 cases, 47, 66, and 28 were classified  
 261 into groups 1–3, respectively. Thus, group 2 had the largest proportion of cases (47%) and  
 262 group 3 had the smallest (20%). The combination of meteorological components in group 1  
 263 indicated the end of a high-pressure system ( $P_{sfc} > 0$ ,  $dP_{sfc}/dt < 0$ ), with southerly winds  
 264 ( $NS850 > 0$ ) bringing warmer air ( $T925 > 0$ ) to the region, leading to stable atmospheric  
 265 stratification and weak surface winds (Fig. 4). This group 1 meteorological mode appeared to  
 266 result in very weak NO<sub>2</sub> ventilation, which produced the highest PC-NO<sub>2</sub> and SI-NO<sub>2</sub> values.  
 267 Group 3 showed the opposite trend, with strong northerly winds bringing colder air into the  
 268 region, leading to an unstable atmosphere and stronger surface winds, and ultimately  
 269 decreasing PC-NO<sub>2</sub> and SI-NO<sub>2</sub> to their lowest levels.

270 SI-NO<sub>2</sub> was approximately twice as high in group 1 than group 3, whereas PC-NO<sub>2</sub>  
 271 showed no significant difference (Fig. 4a). We hypothesized that PBLH might also differ  
 272 significantly under these micrometeorological conditions; therefore, we further explored daily  
 273 maximum PBLH data from Hybrid Single-Particle Lagrangian Integrated Trajectory  
 274 (HYSPLIT) Global Forecast System (GFS) simulations for the 141 cases. The mean simulated  
 275 PBLH was  $942.1 \pm 405.3$  m for 2020, which was similar to the annual mean daily maximum  
 276 PBLH (1,013.6 m) in Osan (Lee et al., 2013). However, the simulated PBLH differed  
 277 significantly among the three groups ( $767.0 \pm 304.8$ ,  $923.2 \pm 335.3$ , and  $1,280.6 \pm 501.2$  m for  
 278 groups 1–3, respectively). The PBLH for group 3 was 1.7-fold higher than that for group 1  
 279 (Fig. 4k). We also detected significant differences among the three groups in synoptic  
 280 components of the lower troposphere including W850, as well as in local meteorological



parameters such as the sea breeze index, which is calculated as  $SBI = U^2/\Delta T$ , where  $U$  is  $W_{sfc}$  (Fig. 4c) and  $\Delta T$  is the temperature difference between  $T_{925}$  and the sea surface temperature. Thus, the SBI represents the ratio between inertial ( $\rho U^2/2$ ) and buoyancy ( $\rho g \beta \Delta T$ ) forces, where  $\rho$  is air density,  $\beta$  is specific heat, and  $g$  is gravity, and its value provides an indication of the likelihood of local circulation events such as sea breezes; at high SBI values, sea breezes cannot overcome the prevailing wind, whereas low SBI values can indicate strong sea breezes. In the example shown in Fig. 4l, the SBI values of groups 1–3 were  $0.1 \pm 4.5$ ,  $0.1 \pm 9.2$ , and  $-0.2 \pm 12.5$ , respectively. Groups 2 and 3 had similar mean SBI values suggesting little local circulation; however, group 1 corresponded to dominant local circulation (LD), group 2 to a mixture of local and synoptic-scale circulation (MD), and group 3 to dominant synoptic-scale circulation (SD). These results indicate that Seosan may experience frequent LD conditions (with sun on one third of the days of the year), with infrequent SD conditions (one fifth of all days).

If the  $NO_2$  profiles are vertically uniform within the PBL (e.g., Fig. 4), the mean SI- $NO_2$  under LD and SD conditions can be scaled to PC- $NO_2$  amounts of 0.87 and 0.90 DU at 1 atm and 298 K, respectively, for the given mean PBLH. The estimated PC- $NO_2$  amounts appeared to be similar across groups, and yet higher than the PC- $NO_2$  observations (0.31 and 0.32 DU, respectively), indicating that  $NO_2$  profile shapes may deviate slightly from the constant vertical shape of the PBL.

300

#### 301 **4.2.1 Relationship between daily mean PC- $NO_2$ and SI- $NO_2$ under LD, MD, and SD** 302 **conditions**

Scatter diagrams of daytime mean PC- $NO_2$  and SI- $NO_2$  measurements at Seosan over the entire 1-year period are shown in Fig. 5. Based on the 141 cases, daytime mean values averaged between 1100 and 1700 KST were used to reduce the effect of nocturnal PBLH variation. Other



306 data selection criteria included concurrent PC-NO<sub>2</sub> and SI-NO<sub>2</sub> measurements, with data  
307 acquisition rates of > 80% per day. Overall, PC-NO<sub>2</sub> and SI-NO<sub>2</sub> were strongly correlated ( $R$   
308 = 0.73; Fig. 5), suggesting that the vertical profiles were generally uniform in the PBL  
309 throughout all four seasons. The slope of the linear regression curve shown in Fig. 5a was 0.02  
310 DU/ppb ( $= 0.53 \times 10^{15}$  molecules cm<sup>-2</sup>/ppb), which is comparable to values ( $0.3\text{--}0.59 \times 10^{15}$   
311 molecules cm<sup>-2</sup>/ppb) obtained previously in a study of surface and OMI-NO<sub>2</sub> measurements  
312 downwind of strong point sources in Israeli cities (Boersma et al., 2009). The intercept (0.17  
313 DU) was within the range of previous Anmyeondo Pandora measurements, suggesting that  
314 intercepts of 0.15–0.2 DU may represent the local background PC-NO<sub>2</sub> amount (including the  
315 stratospheric NO<sub>2</sub>), rather than the influence of local anthropogenic NO<sub>2</sub> emissions.

316 We classified daily averaged PC-NO<sub>2</sub> and SI-NO<sub>2</sub> data according to the three  
317 meteorological conditions (LD, MD, and SD) and detected a weak correlation under LD  
318 conditions (Fig. 5b); the lowest coefficient of determination for the LD condition ( $R^2 = 0.34$ )  
319 was approximately half of those for the MD (0.359) and SD (0.64) conditions, suggesting that  
320 NO<sub>2</sub> vertical profiles were more complex under LD conditions, with anomalous layers.

321

#### 322 4.2.2 Diurnal variations in column-surface NO<sub>2</sub> under LD, MD, and SD conditions

323 Diurnal patterns of PC-NO<sub>2</sub>, SI-NO<sub>2</sub>, and O<sub>3</sub> under SD, MD, and LD conditions are shown in  
324 Fig. 6. Under LD conditions, PC-NO<sub>2</sub> increased from morning to afternoon (Fig. 6a), whereas  
325 under SD conditions, it had a weak morning peak and subsequent decrease until late afternoon  
326 (Fig. 6c). Under MD conditions, PC-NO<sub>2</sub> had one large peak in the morning and a shoulder  
327 peak in the late afternoon (Fig. 6b). However, SI-NO<sub>2</sub> showed nearly identical diurnal patterns  
328 among the three meteorological conditions, with an early-morning peak followed by a second  
329 peak in the late afternoon (Fig. 6d–f). Diurnal patterns of O<sub>3</sub> were strongly associated with O<sub>3</sub>-  
330 NO<sub>2</sub> photochemical reactions under both LD and MD conditions (Fig. 6g–h), whereas no



particular photochemical effects were detected under SD conditions (Fig. 6i).

A simple linear regression was applied to daytime-average (1100–1700LST) measurements of both PC-NO<sub>2</sub> and SI-NO<sub>2</sub> under the three meteorological condition, and yielded correlation coefficients (*R*) of 0.51 and 0.41 for SD and MD conditions, respectively; however, LD conditions produced a significantly lower *R* (0.27). Thus, under SD conditions, strong synoptic winds suppressed PC-NO<sub>2</sub> and SI-NO<sub>2</sub> diurnal fluctuations, rendering them similar to each other. Strong winds also inhibited local effects of O<sub>3</sub> formation on the diurnal variation of PC-NO<sub>2</sub>, and the smaller impact of chemical conversion from local NO<sub>2</sub> to O<sub>3</sub> lowered *R* values during the day. Under MD conditions, both PC-NO<sub>2</sub> and SI-NO<sub>2</sub> exhibited distinctive peaks in the morning with a degree of time lag; both subsequently declined toward noon, and showed higher *R* values than those obtained under SD conditions. By contrast, under MD conditions, correlations were enhanced due to a minimum around 1500 KST for both PC-NO<sub>2</sub> and SI-NO<sub>2</sub>, despite time lags in both peaks in the morning and afternoon.

Previous studies of the Megacity Air Pollution Seoul (MAPS-Seoul) and KORUS-AQ campaigns reported a typical pattern of continuously increasing PC-NO<sub>2</sub> over the Seoul metropolitan area. However, in the current campaign, we found similar results only under LD conditions. The diurnal patterns reported in previous studies were mainly caused by the dominance of NO<sub>2</sub> emission sources over NO<sub>2</sub> losses (Chong et al., 2019; Herman et al., 2018) among several processes associated with NO<sub>2</sub> photochemical loss, including transport and deposition, which were also investigated in specific cases in the current study.

#### 4.3 Aircraft measurements collected during GMAP-2020

Data collected via aircraft during GMAP-2020 are summarized in Table 2. A total of nine aircraft measurements were conducted during the campaign period (November 12, 2020–January 20, 2021). Four of nine flights were conducted under LD conditions, and the remaining



356 flights (except that on November 27, 2020) were conducted under MD conditions. No aircraft  
357 measurements were consistent with SD conditions during the GMAP-2020 campaign.

358 We examined spiral segments from each flight over Seosan during 1100–1700 KST to  
359 exclude marginal effects of diurnal variation in  $\text{NO}_2$  (Fig. 2). The overall results indicated that  
360 the vertical  $\text{O}_3$  profiles were relatively constant in the PBL, whereas  $\text{NO}_2$  profiles appeared to  
361 be highly dependent on meteorological conditions. We compared data collected during flights  
362 conducted under LD (one flight) and MD conditions (two flights) during the GMAP-2020  
363 campaign, to examine differences in the vertical structures of the PA and SI observations.

364 Aircraft measurements of vertical  $\text{NO}_2$  and  $\text{O}_3$  profiles for flights FL-5 (December 6) and  
365 FL-6 (December 8) under LD conditions are shown in Fig. 7, along with 24-h backward  
366 trajectories starting at different altitudes (100, 500, and 1,000 m). All observed  $\text{NO}_2$  profiles  
367 shown in Fig. 7 appeared to have generally exponential curves, with anomalous features at  
368 higher altitudes. For example, when vertical turbulent mixing prevailed within the PBL ( $\text{O}_3$   
369 profile, Fig. 7b), the data were fitted with an exponential vertical curve, and the anomalous  
370  $\text{NO}_2$  layer aloft was found to have a height of 1.5 km, which was higher than the estimated  
371 PBLH of 1.2 km. HYSPLIT 24-h backward trajectories starting at 1200 KST showed that all  
372 air mass from the surface to the lower free atmosphere was transported over the Yellow Sea  
373 via the Shandong Peninsula (Fig. 7c). This finding suggests that the anomalous  $\text{NO}_2$  layer aloft  
374 was not produced locally (i.e., from local LPS emissions), but instead traveled via long-range  
375 regional-scale transport. According to Anmyeondo Lidar measurements for December 6  
376 (<http://kalion.kr>), the anomalous  $\text{NO}_2$  layer aloft corresponded well to an aerosol layer that  
377 appeared at  $\sim 1.0$  km at approximately 1200 KST, persisting until 2200 KST. However, based  
378 on a cross-comparison of our data, high surface levels of SI- $\text{NO}_2$  ( $> \sim 4$  ppb; Fig. 7a) were  
379 influenced more by local LPS than by that in the atmosphere aloft due to long-range transport  
380 (Fig. 7a).





Aircraft measurements for flight FL-7 (December 9) under LD conditions are shown in Fig. 7b. The  $\text{NO}_2$  vertical profile exhibited an exponential curve, with an anomalous peak at ~600 m immediately above the top of the simulated PBL. HYSPLIT backward trajectory data starting at 1200 KST showed that the non-surface air had a different origin from the surface air (Fig. 6d), indicating that the anomalous  $\text{NO}_2$  plume likely traveled from coal-fired power plants in a nearby industrial city (Taean) northwest of Seosan. This finding indicates a distinct vertical structure of higher  $\text{NO}_2$  at the surface due to strong local emissions, whereas lower  $\text{NO}_2$  levels were observed at higher altitudes, with anomalously high  $\text{NO}_2$  levels in some layers aloft due to medium-range transport from nearby areas. Thus, despite the limited number of aircraft measurements, the elevated anomalous  $\text{NO}_2$  structure that was observed intermittently led to a negative correlation between PA- $\text{NO}_2$  and SI- $\text{NO}_2$ . Therefore, GEMS validation should proceed cautiously when only surface measurements alone are obtained under LD meteorological conditions.

Aircraft measurements were conducted under MD conditions on flights FL-1 (November 26), FL-3 (November 28), and FL-8 (December 12) (Fig. 8). We applied several regression models (linear, exponential, and polynomial) to three vertical structures, and obtained two distinct  $\text{NO}_2$  vertical profile patterns from the surface to the PBLH: decreasing linearly for FL-1 and FL-8 (Fig. 8), and constant with altitude for FL-3 (Fig. 8b). None of the three cases showed anomalous layers above the PBLH, similar to the exponentially declining profiles obtained under LD conditions (Fig. 7). These vertical structures observed under MD conditions may have been induced by strong vertical mixing within the PBL, supplemented by prominent surface photochemical losses at the same time. The vertical  $\text{O}_3$  profile during FL-1 showed a decoupled structure, with different patterns within and above the PBL (Fig. 8d); however, the other 2 days showed uniform distributions, with no particular anomalous features between the upper PBL and surface atmosphere (Fig. 8b, c, e, f). The observed daily maximum sensible



406 heat fluxes measured at Seosan (Fig. S1) were much higher for FL-3 ( $175.9 \text{ Wm}^{-2}$ ) than FL-1  
407 and FL-8 (118.9 and  $102.0 \text{ Wm}^{-2}$ ), suggesting that vertical turbulent mixing was much more  
408 prominent during FL-3. These chemical and physical characteristics are all related to MD  
409 conditions. Thus, the higher coefficient of determination ( $R^2 = 0.64$ ) obtained under MD  
410 conditions (Fig. 5b) has an important bearing on the absence of irregular or anomalous layers  
411 aloft, with little variation regardless of the shape of the curve (Figs. 7 and 8).

412

#### 413 **4.4 Analyses of column–surface relationships for specific GMAP-2020 cases**

414 Figure 9 shows examples of PC-NO<sub>2</sub> and SI-NO<sub>2</sub> diurnal variation under LD (FL-5 and FL-7)  
415 and MD (FL-1 and FL-8) conditions, and Fig. 10 shows latitudinal mean distributions for FL-  
416 5 and FL-7, based on the aircraft measurement data shown in Figs. 7 and 8. PC-NO<sub>2</sub> was found  
417 to be decoupled from SI-NO<sub>2</sub> on 2 days, FL-5 and FL-7, which were both classified as having  
418 LD conditions (Fig. 9a, b), whereas good vertical mixing and uniform NO<sub>2</sub> distribution were  
419 observed on the remaining 2 days, FL-1 and FL-8, which showed MD conditions (Fig. 9c, d).  
420 According to our analysis of the aircraft measurements (Fig. 7), the poor correlations between  
421 PC-NO<sub>2</sub> and SI-NO<sub>2</sub> captured by FL-5 and FL-7 were mainly due to an NO<sub>2</sub> polluted layer  
422 transported aloft, as described in Section 4.3.

423

##### 424 **4.4.1 LD conditions**

425 Several cases showed poor correlation between PC-NO<sub>2</sub> and SI-NO<sub>2</sub> under LD conditions  
426 within the study period. When we examined the results of previous studies (Thompson et al.,  
427 2019; Kim et al., 2021; Chong et al., 2019; Herman et al., 2018), we first considered the  
428 possibility that LPS emissions influenced downwind regions under LD conditions, because the  
429 increase in PC-NO<sub>2</sub> (but not SI-NO<sub>2</sub>) may have required an additional source of NO<sub>2</sub> apart  
430 from early afternoon traffic emissions. The FL-5 data for December 6 represent an example of



431 this, showing a poor correlation between PC-NO<sub>2</sub> and SI-NO<sub>2</sub> ( $R^2 = 0.06$ ; Fig. 9a). On the same  
 432 day, Anmyundo LIDAR detected two elevated aerosol layers at 1200 and 1600–2200 KST  
 433 (<http://kalion.kr>); the first aerosol layer may reflect a PC-NO<sub>2</sub> peak, as shown in Fig. 9a. The  
 434 HYSPLIT backward trajectories, starting at different altitudes from the surface to the lower  
 435 troposphere, revealed that all air parcels moved eastward from China to Anmyundo and Seosan  
 436 (Figure 1); thus, other NO<sub>2</sub> plumes may have begun to pass over Seosan at 1600 KST (Fig. 7c).  
 437 Longitudinal SI-NO<sub>2</sub> distributions (Fig. 10) exhibited 5.2 ppb at 126.1°E, 8.1 ppb at 126.3°E,  
 438 and 7.3 ppb at 126.4°E, averaged between 1300 and 1600 KST by longitude (Table S1),  
 439 whereas they were nearly constant at a height of 500–600 m on December 6. Therefore,  
 440 westerly winds advected cleaner air from Padori (AQMI) to Seosan at the surface, but not at a  
 441 height of 500–600 m, contributing to low SI-NO<sub>2</sub> levels in the afternoon (Fig. 9a).

442 Another example of a weak correlation was obtained by flight FL-7 (December 9), as  
 443 shown in Fig. 9b. Time series PC-NO<sub>2</sub> data exhibited several peaks during 1200–1400 KST  
 444 (Fig. 9b), whereas SI-NO<sub>2</sub> showed less temporal variation, resulting in a weak correlation ( $R =$   
 445  $-0.24$ ) compared with the overall daytime (1100–1700 KST) correlation ( $R^2 = 0.53$ ; Fig. 5a).  
 446 Latitudinal NO<sub>2</sub> levels at high altitudes of ~600 m (Fig. 10b) gradually increased northward,  
 447 whereas surface NO<sub>2</sub> was minimal at the midpoint. For example, at high altitudes, the  
 448 latitudinal mean NO<sub>2</sub> levels were 1.4 ppb (36.8°N), 4.1 ppb (36.9°N), and 5.1 ppb (37.0°N),  
 449 whereas the SI-NO<sub>2</sub> levels at the same sites were 18.0 ppb (36.8°N), 14.3 ppb (36.9°N), and  
 450 16.8 ppb (37.0°N), respectively, averaged during 1200–1400 KST by latitude (Table S1). This  
 451 finding is attributable to a prevailing north wind that transported NO<sub>2</sub> southward at high  
 452 altitudes, while simultaneously ventilating SI-NO<sub>2</sub> toward outer Seosan, resulting in the  
 453 development of several PC-NO<sub>2</sub> peaks. In contrast, SI-NO<sub>2</sub> decreased slowly (Figs. 9b and  
 454 10b).

455



#### 4.4.2 MD and SD conditions

We obtained higher PC–SI correlation coefficients under MD and SD conditions than LD conditions (Figs. 5b and 9c, d). Under MD and SD conditions, diurnal variation in PC-NO<sub>2</sub> and SI-NO<sub>2</sub> showed simultaneous declines from early morning until noon (Fig. 6). Notably, PC-NO<sub>2</sub> showed a continuously decreasing trend, particularly during the morning hours, in the period of approximately 0900–1200 KST under both MD and SD conditions (Fig. 6b, c). These diurnal patterns of decreasing PC-NO<sub>2</sub> in the study area were opposite to those reported in previous studies (Chong et al., 2019; Herman et al., 2018) that observed increasing PC-NO<sub>2</sub> in large urban areas during the daytime, caused by higher NO<sub>2</sub> emissions even during photochemical NO<sub>2</sub> losses to form O<sub>3</sub>.

In this study, we hypothesized that decreasing PC-NO<sub>2</sub> can occur due to photochemical loss and surface wind transport, which both intensify with increasing solar radiation in the morning. Photochemically, NO<sub>2</sub> is converted into photochemical oxidants such as PAN, HNO<sub>3</sub>, and nitrate under sunlight, thereby disrupting the NO<sub>x</sub>–VOC–O<sub>3</sub> cycle. Concurrently, W<sub>sfc</sub> intensified due to thermal turbulence transport of NO<sub>2</sub> emissions away from Seosan during the day. Thus, PC-NO<sub>2</sub> decreases under MD conditions as a result of ventilation effects caused by stronger wind speeds. There are two possible mechanisms for this: sea breeze penetration (because the study area is adjacent to the northern coast of the Taean Peninsula; Fig. 1) and vigorous turbulent mixing (which leads to vertical mixing of surface NO<sub>2</sub> during PBL growth; Sun et al., 2013). We investigated these factors in detail for specific cases.

Figure 11 shows the diurnal variation in selected meteorological and chemical variables measured under MD (November 25) and SD conditions (December 14). Under MD conditions (Fig. 11a–c), declines in PC-NO<sub>2</sub> and SI-NO<sub>2</sub> were observed toward noon. In particular, decreasing PC-NO<sub>2</sub> was accompanied by increased W<sub>sfc</sub> (Fig. 11b); therefore, we examined GMAP-2020 campaign measurements of sea breeze penetration.



481 Figure S2a shows diurnal variation in observed air temperatures at site Met<sub>1</sub> and  
482 measured sea surface temperatures at nearby site Met<sub>2</sub> (37.14°N, 126.01°E), located 55 km  
483 from PA<sub>4</sub>. The thermal meteorological observations were used to calculate SBI (+0.37), which  
484 was greater than +3 (the threshold for sea breeze occurrence; Brigges and Graves, 1962). Sea  
485 breeze disturbances with a sharp decrease (increase) in temperature (humidity) were observed  
486 at site Met<sub>3</sub> (Fig. S2b), which is located on the northern coastline of Taean Peninsula (Fig. 1).  
487 However, sea breezes did not progress inland at the Met<sub>1</sub> Seosan Meteorological Automated  
488 Surface Observing System (ASOS) site, which is closer to the Pandora sites; sea breezes did  
489 not correlate with NO<sub>2</sub> ventilation to offset its high emission.

490 We further detected a strong positive correlation between wind speed and sensible heat  
491 flux (Fig. 11b). We speculated that thermal and momentum turbulences caused by a vertical  
492 temperature gradient and surface friction entrained surface turbulence, thus increasing  
493 momentum in the free atmosphere downward to the surface due to strong turbulent mixing  
494 within the PBL, in turn leading to a uniform vertical NO<sub>2</sub> profile with a positive correlation  
495 between PC-NO<sub>2</sub> and SI-NO<sub>2</sub>. Figure S3 shows a comparison of daily maximum sensible heat  
496 and momentum fluxes under LD, MD, and SD conditions during the GMAP-2020 campaign.  
497 SD conditions showed the highest mean heat flux, followed by MD and LD, indicating that  
498 downward momentum transport led by both heat and momentum fluxes plays a greater role in  
499 Wsfc enhancement under MD than LD conditions within the PBL.

500 Photolytic NO<sub>2</sub> loss was detected as temporal variations in NO<sub>2</sub>, NO<sub>3</sub><sup>-</sup>, and CO at PA<sub>4</sub>.  
501 Because no NO<sub>2</sub> analyzer was installed at PA<sub>4</sub>, NO<sub>2</sub><sup>\*</sup>(= NO<sub>y</sub> – NO) was used instead of NO<sub>2</sub>  
502 under the assumption that NO<sub>x</sub> is negligible in winter. Figure 11c shows the diurnal variation  
503 in NO<sub>2</sub>, O<sub>3</sub>, and NO<sub>3</sub><sup>-</sup> under MD conditions, normalized by CO to reduce the effect of PBL  
504 evolution. The results showed that NO<sub>2</sub>/CO decreased after the morning peak; however, NO<sub>3</sub><sup>-</sup>  
505 /CO and O<sub>3</sub>/CO increased toward midday, indicating that photolytic activity also contributed



considerably to the concurrent decline of SI-NO<sub>2</sub> and PC-NO<sub>2</sub> (Fig. 11a). In turn, this indicated that photochemistry can contribute to higher correlation coefficients under MD conditions.

Under SD conditions (Fig. 11d–f), PA-NO<sub>2</sub> and SI-NO<sub>2</sub> exhibited weak diurnal variability compared with LD and MD conditions. SD conditions on December 14 produced significantly stronger winds (i.e., wind speed > 6 m s<sup>-1</sup> at 1300 KST), with generally higher PBLHs (Fig. 11e). Meteorological features, such as strong wind at both 850 hPa (18.0 m s<sup>-1</sup>) and 10 m height (4.26 m s<sup>-1</sup>), suppressed both PC-NO<sub>2</sub> and SI-NO<sub>2</sub> (7.3 ppb and 0.31 DU, respectively) to below the average, producing a strong correlation ( $R = 0.9$  at AQM<sub>5</sub>) and nearly flattening their temporal curves during the day (Fig. 11d). Thus, under SD conditions, wind speed and turbulent fluxes such as sensible heat flux had larger values, and NO<sub>2</sub> and NO<sub>3</sub><sup>-</sup> decreased or increased at the same time during the day (Fig. 11f), indicating that the transport effect was much greater than that of local photochemical loss over the study area.

In conclusion, in this case-specific study, we discussed correlations between PC-NO<sub>2</sub> and SI-NO<sub>2</sub>, and explored their mechanisms by investigating the impact of meteorological and photochemical conditions. A weak correlation between PC-NO<sub>2</sub> and SI-NO<sub>2</sub> occurred when anomalously high concentrations remained, with ragged fragments of NO<sub>2</sub> plumes in the upper or middle layers. We also found that a negative correlation occurred intermittently under LD conditions, with generally lower PBLH. In particular, elevated pollutant levels due to regional-scale transport or decoupled NO<sub>2</sub> plumes advected within the PBL may also have caused the weak correlation between PC-NO<sub>2</sub> vs. SI-NO<sub>2</sub>. These phenomena were detected only from the PA–SI coupled measurements in this study. Thus, when either PC or SI observations are applied alone for GEMS validation, undetected bias can occur under LD conditions, particularly where transport processes prevail.

529

## 5. Conclusions



531 In this study, we explored the potential applicability of combined PC-NO<sub>2</sub> and SI-NO<sub>2</sub>  
532 measurements collected at Seosan during the GMAP-2020 campaign. We characterized the  
533 correlation between PC-NO<sub>2</sub> and SI-NO<sub>2</sub> under various conditions to understand the complex  
534 air quality of Seosan, which appears to be vulnerable to LPS emissions from surrounding areas.  
535 We hypothesized that correlations between PC-NO<sub>2</sub> and SI-NO<sub>2</sub> are closely related to NO<sub>2</sub>  
536 vertical profiles, which also depend on meteorological conditions. We performed statistical  
537 analyses of a year-long PC-NO<sub>2</sub> dataset (November 12, 2020–October 30, 2021) combined  
538 with meteorological data, *in situ* ground data, and airborne chemical data measured during the  
539 GMAP-2020 campaign in the same period.

540 Our results showed that hourly PC-NO<sub>2</sub> and SI-NO<sub>2</sub> over the 1-year period exhibited a  
541 logarithmic relationship with a fair correlation ( $R = 0.45$ ), and the intercept of the logarithm  
542 regression line (corresponding to zero-surface NO<sub>2</sub>) was 0.09 DU, consistent with the  
543 stratospheric column NO<sub>2</sub> amounts retrieved by TROPOMI. Daily mean PC-NO<sub>2</sub> and SI-NO<sub>2</sub>  
544 exhibited a good linear correlation ( $R = 0.73$ ), supporting the overall uniformity of NO<sub>2</sub> profiles  
545 in the PBL over Seosan despite the continuous impact of LPS emissions.

546 The impact of meteorological conditions on the relationship between PC-NO<sub>2</sub> and SI-  
547 NO<sub>2</sub> was investigated through agglomerative hierarchical clustering, which indicated three  
548 meteorological conditions: LD, MD, and SD. Under LD conditions, southerly winds advect  
549 warm air under the upper ridge, forming stable and short PBLs and weak surface winds. By  
550 contrast, under SD conditions, cold northerly winds induce unstable and high PBLs with strong  
551 surface winds. The correlations between daily mean PC-NO<sub>2</sub> and SI-NO<sub>2</sub> levels, and their  
552 variations during 1100–1700 KST, weakened under LD conditions, suggesting that the shape  
553 of the NO<sub>2</sub> profile typically deviates from a uniform profile under SD and MD conditions.  
554 Aircraft measurements under LD conditions demonstrated NO<sub>2</sub> plumes aloft, with anomalous  
555 vertical structures and different horizontal (latitudinal) gradients of surface NO<sub>2</sub> at higher



altitudes, such as 600 m over Seosan.

Thus, the relationship between PC-NO<sub>2</sub> and SI-NO<sub>2</sub> depends on the presence of NO<sub>2</sub> plumes aloft under LD conditions, which provide a favorable environment for LPS plumes decoupled from the surface at Seosan. The findings of this study suggest that the correlation of PC-NO<sub>2</sub> and SI-NO<sub>2</sub> may serve as an indicator of the degree of complexity of urban air quality. This correlation can be optimally applied for air quality evaluation and environmental satellite validation by combining the Pandora Asia Network with AQM networks. More detailed studies on urban air pollution evaluation will be undertaken based on PC, DOAS, aircraft, SI air quality, and surface turbulence observation data, as well as modeling studies of data collected during the GMAP-2021 campaign.

#### Acknowledgments

We thank all those who contributed to the GMAP-2020 field campaign, and PGN for raw data processing.

#### Funding

This study was supported by the National Institute of Environmental Research (NIER-2021-01-01-052 and NIER-2021-03-03-001), and was partially supported by National Research Foundation of Korea (NRF) funded by the Ministry of Education of the Republic of Korea (Grant No. 2020R1A6A1A03044834)

#### Data Availability

#### Author Contributions:





580 Lim-Seok Chang: Conceptualization, Formal analysis, Visualization, Investigation, Writing -  
 581 Original draft; Donghee Kim, Hyunkee Hong, Deok-Rae Kim, Jeonga Yu, and Daewon Kim; Data  
 582 curation; Hanlim Lee, Kwangyul Lee, and Jinkyu Hong: Methodology and formal analysis; Hyun-  
 583 Young Jo: Formal analysis and Visualization; Cheol-Hee Kim ; Writing—original draft preparation,  
 584 Writing—review and editing. All authors have read and agreed to the published version of the  
 585 manuscript

586

## 587 **References**

- 588 NIER-GP2021-002, 2021. Air Quality Monitoring Network Installation and Operation. Ministry of the  
 589 Environment.
- 590 Biggs, W.G., Graves, M.E., 1972. A lake breeze index. J. Appl. Meteor. 1, 474–480.
- 591 Boersma, K.F., Jacob, D.J., Trainic, M., Rudich, Y., DeSmedt, I., Dirksen, R., Eskes, H.J., 2009.  
 592 Validation of urban NO<sub>2</sub> concentrations and their diurnal and seasonal variations observed  
 593 from the SCIAMACHY and OMI sensors using in situ surface measurements in Israeli cities.  
 594 Atmos. Chem. Phys. 9, 3867–3879. <https://doi.org/10.5194/acp-9-3867-2009>.
- 595 Bouchlaghem, K., Mansour, F.B., Elouragini, S., 2007. Impact of a sea breeze event on air pollution at  
 596 the Eastern Tunisian Coast. Atmos. Res. 86, 162–172.
- 597 Cede, 2019. A: Manual for Blick software Suite 1.6.  
 598 [http://pandonia.net/media/documents/BlickSoftwareSuite\\_Manual\\_v11.pdf](http://pandonia.net/media/documents/BlickSoftwareSuite_Manual_v11.pdf).
- 599 Chong, H., Lee, H., Koo, J.H., Kim, J., Jeong, U., Kim, W., Kim, S.W., Herman, J.R., Abuhassan, N.K.,  
 600 Ahn, J.Y., Park, J.H., Kim, S.K., Moon, K.J., Choi, W.J., Park, S.S., 2019. Regional characteristics  
 601 of NO<sub>2</sub> column densities from Pandora observations during the MAPS-Seoul campaign. Aerosol  
 602 Air Qual. Res. 18, 2207–2219.
- 603 Engel-Cox, J.A., Holloman, C.H., Coutant, B.W., Hoff, R.M., 2004. Qualitative and quantitative



- 604 evaluation of MODIS satellite sensor data for regional and urban scale air quality. *Atmos. Environ.*  
 605 38, 2495–2509.
- 606 Flynn, C.M., Pickering, K.E., Crawford, J.H., Weinheimer, A.J., Diskin, G., Thornhill, K.L., Loughner,  
 607 C., Lee, P., Strode, S.A., 2016. Variability of O<sub>3</sub> and NO<sub>2</sub> profile shapes during DISCover-AQ:  
 608 Implications for satellite observations and comparisons to model-simulated profiles. *Atmos.*  
 609 *Environ.* 147, 133–156.
- 610 Herman, J., Cede, A., Spinei, E., Mount, G., Tzortziou, M., Abuhassan, N., 2009. NO<sub>2</sub> column amounts  
 611 from ground-based Pandora and MFDOAS spectrometers using the direct-sun DOAS technique,  
 612 Intercomparisons and application to OMI validation. *J. Geophys. Res. Atmos.* 114, (D13307).
- 613 Herman, J., Spinei, E., Fried, A., Kim, J., Kim, J., Kim, W., Cede, A., Abuhassan, N., Rozenhaimer,  
 614 S.M., 2018. NO<sub>2</sub> and HCHO measurements in Korea from 2012 to 2016 from Pandora spectrometer  
 615 instruments compared with OMI retrievals and with aircraft measurements during the KORUS-AQ  
 616 campaign. *Atmos. Meas. Tech.* 11, 4583–4603.
- 617 Hong, J.-W., Lee, S.-D., Lee, K., Hong, J., 2019. Seasonal variations in the surface energy and CO<sub>2</sub>  
 618 flux over a high-rise, high-population, residential urban area in the East Asian monsoon region. *Int.*  
 619 *J. Climatol.* 40, 4384–4407.
- 620 Kim, J., Jeong, U., Ahn, M.-H., Park, R.J., Lee, H., Song, C.H., Choi, Y.-S., Lee, K.-H. Yoo, J.-M.,  
 621 Jeong, M.-J. Park, S.K., Lee, K.-M., Song, C.-K., Kim, S.-W., Kim, Y.J., Kim, S.-W., Kim, M., Go,  
 622 S., Liu, X., Chance, K., Miller, C.C., Al-Saadi, J., Veihelmann, B., Bhartia, P.K., Torres, O., Abad,  
 623 G.G., Haffner, D.P., Ko, D.H., Lee, S.H., Woo, J.-H., Chong, H., Park, S.S., Micks, D., Choi, W.J.,  
 624 Moon, K.-J., Veefkind, P., Levelt, P.F., Edwards, D.P., Kang, M., Eo, M., Bak, J., Baek, K., Kwon,  
 625 H.-A., Yang, J., Park, J., Han, K.M., Kim, B.-R., Shin, H.-W., Choi, H., Lee, E., Chong, J., Cha, Y.,  
 626 Koo, J.-H., Hayashida, S., Kasai, Y., Kanaya, Y., Liu, C., Lin, J., Crawford, J.H., Carmichael, G.R.,  
 627 Newchurch, M., J., Lefer, B.L., Herman, J.R., Swap, R.J., Lau, A.K.H., Kurosu, T.P., Jaross, G.,  
 628 Ahlers, B., Dobber, M., McElroy, T.C., Choi, Y., 2020. New era of air quality monitoring from



- 629 space: Geostationary Environment Monitoring Spectrometer (GEMS). BAMS 101, E1–E22.  
 630 <https://doi.org/10.1175/BAMS-D-18-0013.1>.
- 631 Kim, S.-M. Koo, J.-H. Lee, H.; Mok, J.; Choi, M. Go, S., Lee, S. Cho, Y. Hong, J. Seo, S., 2021  
 632 Comparison of PM<sub>2.5</sub> in Seoul, Korea Estimated from the Various Ground-Based and Satellite  
 633 AOD. Appl. Sci. 11, 10755.
- 634 Kim, S.U., Kim, K.Y., 2020. Physical and chemical mechanisms of the daily-to-seasonal variation of  
 635 PM<sub>10</sub> in Korea. Sci. Total Environ. 712, 136429. <https://doi.org/10.1016/j.scitotenv.2019.136429>.
- 636 Lamsal, L.N., Martin, R.V., van Donkelaar, A., Celarier, E.A., Bucsela, E.J., Boersma, K.F., Dirksen,  
 637 R., Luo, C., Wang, Y., 2010. Indirect validation of tropospheric nitrogen dioxide retrieved from the  
 638 OMI satellite instrument: Insight into the seasonal variation of nitrogen oxides at northern  
 639 midlatitudes. J. Geophys. Res. 115, D05302. doi:[10.1029/2009JD013351](https://doi.org/10.1029/2009JD013351).
- 640 Lee, S., Kim, M., Kim, S.Y., Lee, D.W., Lee, H., Kim, J., Le, S., Liu, Y., 2021. Assessment of long-  
 641 range transboundary aerosols in Seoul, South Korea from Geostationary Ocean Color Imager  
 642 (GOCI) and ground-based observations. Environ. Pollut. 269, 115924.
- 643 Lee, S.J., Lee, J., Greybush, S.J., Kang, M., Kim, J., 2013. Spatial and temporal variation in PBL height  
 644 over the Korean Peninsula in the KMA operational regional model, Adv. Meteorol. ID. [381630](https://doi.org/10.1016/j.admet.2013.06.001).
- 645 Lim, H.-J., Lee, Y.-H., 2019. Characteristics of sea breezes at coastal area in Boseong. Atmos. Korean  
 646 Meteorological. Society. 29, 41–51.
- 647 Sun, J., Lenschow, D.H., Mahrt, L., Nappo, C., 2013. The relationships among wind, horizontal  
 648 pressure gradient, and turbulent momentum transport during CASES-99. J. Atmos. Sci. 70, 3397–  
 649 3414.
- 650 Thompson, A.M., Stauffer, R.M., Boyle, T.P., Kollonige, D.E., Miyazaki, K., Tzortziou, M., Herman,  
 651 J.R., Abuhassan, N., Jordan, C.E., Lamb, B.T., 2019. Comparison of near-surface NO<sub>2</sub> pollution  
 652 with Pandora total column NO<sub>2</sub> during the Korea-United States Ocean Color (KORUS OC)



- 653 Campaign. J. Geophys. Res. Atmos.. 124, 13560–13575. [10.1029/2019JD030765](https://doi.org/10.1029/2019JD030765).
- 654 Van Roozendaal, M., Fayt, C., 2001. WinDOAS 2.1 Software user manual, Uccle. 920 IASB/BIRA.
- 655 Wang, J., Christopher, S.A., 2003. Intercomparison between satellite-derived aerosol optical  
656 thickness and PM<sub>2.5</sub> mass: Implications for air quality studies. Geophys. Res. Lett. 30, 2095.  
657 doi:[10.1029/2003GL018174](https://doi.org/10.1029/2003GL018174).
- 658 Wang, Y., Dörner, S., Donner, S., Böhnke, S., Smedt, I.D., Dickerson, R.R., Dong, Z., He, H., Li, Z.,  
659 Li, D., Ren, X., Theys, N., Wang, Y., Wang, Z., Xu, H., Xu, J., Wagner, T., 2019. Vertical profiles  
660 of NO<sub>2</sub>, SO<sub>2</sub>, HONO, HCHO, CHOCHO and aerosols derived from MAX-DOAS measurements at  
661 a rural site in the central western North China Plain and their relation to emission sources and effects  
662 of regional transport. Atmos. Chem. Phys. 19, 5417–5449.
- 663
- 664
- 665
- 666
- 667
- 668
- 669
- 670
- 671
- 672
- 673
- 674
- 675
- 676



## List of Tables

**Table 1.** Summary of NO<sub>2</sub> column data from four Pandora (PA) measurement sites.

**Table 2.** Summary of aircraft measurements collected during the Geostationary Environment Monitoring Spectrometer (GEMS) Map of Air Pollution (GMAP)-2020 campaign period (November 12, 2020–January 20, 2021).

**Table 1.** Summary of NO<sub>2</sub> column data from four Pandora (PA) measurement sites.

Site	Site name	Site location		Mean (DU)	SD (DU)	Minimum (DU)	Maximum (DU)	Number of data points (days)	Operating period
		Longitude (°E)	Latitude (°N)						
PA <sub>1</sub>	Seosan-DHJ	126.502	36.900	0.50	0.22	0.20	1.60	838 (11)	GMAP-2020 campaign
PA <sub>2</sub>	Seosan-DM	126.458	36.778	0.43	0.19	0.18	1.62	1241 (13)	GMAP-2020 campaign
PA <sub>3</sub>	Seosan-CC	126.449	36.785	0.40	0.14	0.18	0.97	1242 (13)	GMAP-2020 campaign
PA <sub>4</sub>	Seosan-SS	127.492	36.777	0.39	0.16	0.17	1.79	8753 (141)*	1 year (Nov. 12, 2020–Oct. 30, 2021)

\* The Pandonia Global Network (PGN) retrieval algorithm was applied to yearly measurements.



**Table 2.** Summary of aircraft measurements collected during the Geostationary Environment Monitoring Spectrometer (GEMS) Map of Air Pollution (GMAP)-2020 campaign period (November 12, 2020–January 20, 2021).

Flight no.	Date	Meteorological classification
FL-1	Nov. 26, 2020	MD <sup>1)</sup>
FL-2	Nov. 27, 2020	No Pandora measurements
FL-3	Nov. 28, 2020	MD
FL-4	Dec. 1, 2020	LD <sup>2)</sup>
FL-5	Dec. 6, 2020	LD
FL-6	Dec. 8, 2020	LD
FL-7	Dec. 9, 2020	LD
FL-8	Dec. 12, 2020 (am)	MD
FL-9	Dec. 12, 2020 (pm)	MD

<sup>1)</sup> LD: local wind-dominant conditions; <sup>2)</sup> MD: mixed conditions.



## Figure Captions

705

706 **Figure 1.** Map of sites used for Geostationary Environment Monitoring Spectrometer (GEMS)  
 707 Map of Air Pollution (GMAP) campaigns conducted in (left) Seosan, South Korea in  
 708 November 2020 to January 2021 (GMAP-2020), and (right) the Seoul metropolitan area from  
 709 October 2021 to November 2021 (GMAP-2021). (Left) Measurement sites around Seosan, the  
 710 study area for the GMAP-2020 campaign. Red circles indicate Pandora column measurement  
 711 sites including (left) Seosan Daehoji (PA<sub>1</sub>), Seosan Dongmun (PA<sub>2</sub>), Seosan City Council  
 712 (PA<sub>3</sub>), and Seosan Super Site (PA<sub>4</sub>). Blue triangles indicate large point sources (LPSs)  
 713 including the Taean and Dangjin thermal power stations (LPS<sub>1</sub> and LPS<sub>2</sub>, respectively),  
 714 Hyundai steelworks (LPS<sub>3</sub>), and Daesan petrochemical complex (LPS<sub>4</sub>). Yellow squares  
 715 indicate Automated Synoptic Observing System meteorological sites in Seosan (Met<sub>1</sub>), AWS  
 716 (Met<sub>2</sub>), and buoy (Met<sub>3</sub>). Green squares indicate air quality monitoring (AQM) network  
 717 stations including Padori (AQM<sub>1</sub>), Leewon (AQM<sub>2</sub>), Taean (AQM<sub>3</sub>), Daesan (AQM<sub>4</sub>),  
 718 Seongyeon (AQM<sub>5</sub>), and Dongmoon (AQM<sub>6</sub>). In the right panel, the black line indicates the  
 719 route used for car-based differential optical absorption spectroscopy (Car-DOAS)  
 720 measurements and the blue dotted line indicates the horizontal domain of Geo-CAPE airborne  
 721 simulator (GCAS) measurements taken during the GMAP-2021 campaign.

722

723 **Figure 2.** Flight tracks for two Cessna Grand Caravan 208 B aircraft over Pandora sites (left)  
 724 PA<sub>4</sub> and (right) PA<sub>1</sub> during the GMAP-2020 campaign. Colored circles indicate airborne NO<sub>2</sub>  
 725 concentration observations. Stacked circles indicate spiral flights conducted over two sites.

726

727 **Figure 3.** a) Pandora column (PC) NO<sub>2</sub> measurements as a function of surface *in situ* (SI) NO<sub>2</sub>  
 728 observations at Pandora sites PA<sub>1</sub>–PA<sub>3</sub> during the GMAP-2020 campaign and PA<sub>4</sub> during a 1-  
 729 year period. A logarithmic regression model was used to evaluate the relationship between PC  
 730 and SI measurements (black line). (b) Sample scatter plots of PC-NO<sub>2</sub> and SI-NO<sub>2</sub> for February  
 731 24 (red) and April 21 (blue), 2021.

732

733 **Figure 4.** K-means clustering yielded three groups of cases for (a) surface NO<sub>2</sub> and (b) PC-  
 734 NO<sub>2</sub>, associated with eight meteorological variables: (c) surface wind speed (Wsfc), (d) Psfc,  
 735 (e) Psfc tendency (dPsfc/dt), (f) 925-hPa air temperature (T925), (g) 850-hPa wind speed



(W850), (h) 850-hPa north–south wind component (NS850), (i) 850-hPa east–west wind component (EW850), and (j) 500-hPa geopotential height (GPH500). All data were de-seasonalized using the 30-day moving average, except PC-NO<sub>2</sub>, for which the monthly average was used. (k) Simulated daily maximum mixing height (not directly clustered). (l) Box and whisker plots of the sea breeze index (SBI) at Seosan for the 1-year period. Red dots indicate critical SBI values (3: Biggs and Graves, 1962).

742

**Figure 5.** Scatter plots of daytime mean PC-NO<sub>2</sub> vs. SI-NO<sub>2</sub> measurements at site PA<sub>4</sub> under (a) all meteorological conditions and (b) each meteorological condition over a period of 1 year (November 12, 2020–October 30, 2021).

746

**Figure 6.** Box and whisker plots of diurnal variations in (a–c) PC-NO<sub>2</sub>, (d–f) SI-NO<sub>2</sub>, and (g–i) surface O<sub>3</sub> under synoptic wind-dominant (SD), mixed (MD), and local wind-dominant (LD) conditions in Seosan during a 1-year period (November 12, 2020–October 30, 2021).

750

**Figure 7.** Box and whisker plots of the vertical NO<sub>2</sub> and O<sub>3</sub> profiles measured by GMAP aircraft superposed with *in situ* AQMS<sub>1</sub> measurements during flights (a, b) FL-1 (November 26) and (d, e) FL-8 (December 12). Blue dashed lines are linear regression lines fitted to NO<sub>2</sub> and O<sub>3</sub> profiles within the planetary boundary layer (PBL). Black arrows indicate the simulated PBL height (PBLH) obtained from the Korea Meteorological Administration (KMA). HSYPLIT 24-h backward trajectories in Seosan are shown at altitudes of 100, 500, and 1,000 m, starting at 1600 KST on November 26 and 1200 KST on December 12.

758

**Figure 8.** Box and whisker plots of vertical profiles obtained from GMAP aircraft superposed with *in situ* AQMS measurements for (1) NO<sub>2</sub> and (2) O<sub>3</sub> for flights (a) FL-1 (November 26), (b) FL-3 (November 28), and (c) FL-8 (December 12). Blue dashed lines are linear regression lines fitted to NO<sub>2</sub> and O<sub>3</sub> in the PBL. Black arrows indicate PBLH simulated by the Hybrid Single-Particle Lagrangian Integrated Trajectory (HYSPLIT) Global Forecast System (GFS).

764

**Figure 9.** Time series and scatter plots of PC-NO<sub>2</sub> and SI-NO<sub>2</sub> at PA<sub>2</sub> on (a) December 6, (b) December 9, (c) November 26, and (d) December 12. (e) Scatter plot of PC-NO<sub>2</sub> and SI-NO<sub>2</sub> on December 6 (blue), December 9 (red), November 26 (gray), and December 12 (black). (f) Vertical potential temperature profiles on December 6, 9, and 12, 2020. Radiosonde data for November 26, 2020 are missing.





770  
771 **Figure 10.** Latitudinal  $\text{NO}_2$  distribution at the surface and 600 m over  $\text{PA}_4$  (Seosan Super Site),  
772 averaged during (a) 1300–1600 KST on December 6 (FL-5) by longitude and (b) 1200–1400  
773 KST on December 9 (FL-7) by latitude, obtained from airborne (blue) and surface  
774 measurements (red).

775  
776 **Figure 11.** Example of diurnal variations on November 25 (a, c) and December 14 (d, f). (a, d)  
777 Column  $\text{NO}_2$  at sites  $\text{PA}_1$ – $\text{PA}_4$  and surface  $\text{NO}_2$  at the air quality monitoring sites  $\text{AQM}_4$  and  
778  $\text{AQM}_6$ . (b, e) Sensible heat fluxes and surface wind speed at  $\text{PA}_4$ . (c, f) Diurnal variations in  
779  $\text{NO}_2$ ,  $\text{NO}_2^-$ , and  $\text{O}_3$  normalized by  $\text{CO}$ . A map of the measurement sites is shown in Figure 1.

780

781

782

783

784

785

786

787

788

789

790

791

792

793

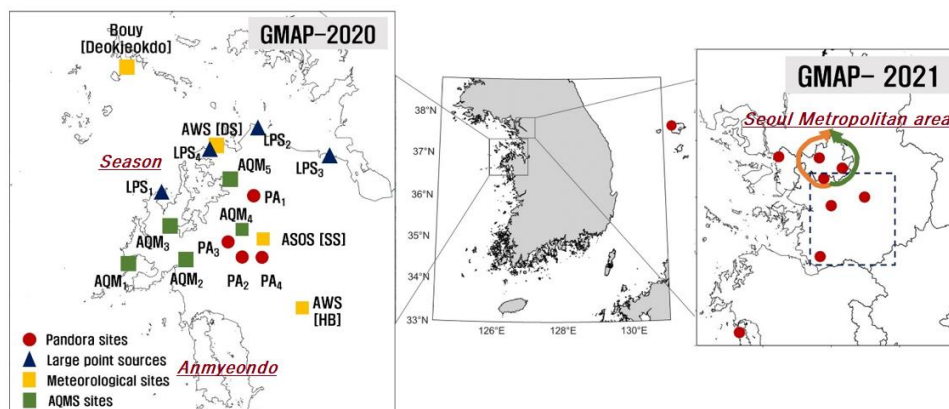
794

795



796

797



798

799

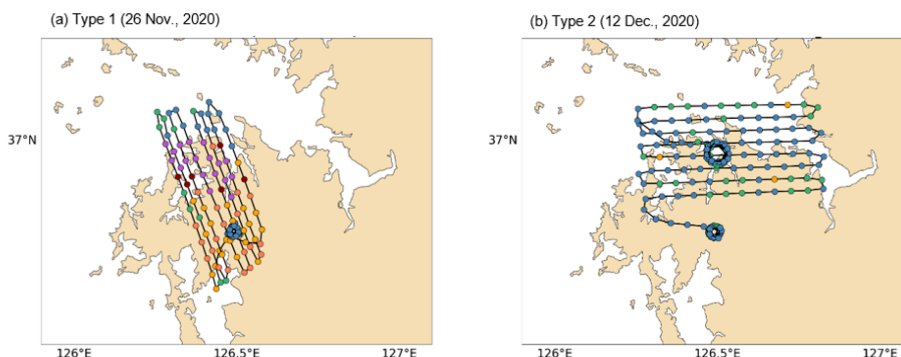
**Figure 1.** Map of sites used for Geostationary Environment Monitoring Spectrometer (GEMS) Map of Air Pollution (GMAP) campaigns conducted in (left) Seosan, South Korea in November 2020 to January 2021 (GMAP-2020), and (right) the Seoul metropolitan area from October 2021 to November 2021 (GMAP-2021). (Left) Measurement sites around Seosan, the study area for the GMAP-2020 campaign. Red circles indicate Pandora column measurement sites including (left) Seosan Daehoji (PA<sub>1</sub>), Seosan Dongmun (PA<sub>2</sub>), Seosan City Council (PA<sub>3</sub>), and Seosan Super Site (PA<sub>4</sub>). Blue triangles indicate large point sources (LPSs) including the Taean and Dangjin thermal power stations (LPS<sub>1</sub> and LPS<sub>2</sub>, respectively), Hyundai steelworks (LPS<sub>3</sub>), and Daesan petrochemical complex (LPS<sub>4</sub>). Yellow squares indicate Automated Synoptic Observing System meteorological sites in Seosan (Met<sub>1</sub>), AWS (Met<sub>2</sub>), and buoy (Met<sub>3</sub>). Green squares indicate air quality monitoring (AQMS) network stations including Padori (AQMS<sub>1</sub>), Leewon (AQMS<sub>2</sub>), Taean (AQMS<sub>3</sub>), Daesan (AQMS<sub>4</sub>), Seongyeon (AQMS<sub>5</sub>), and Dongmoon (AQMS<sub>6</sub>). In the right panel, the black line indicates the route used for car-based differential optical absorption spectroscopy (Car-DOAS) measurements and the blue dotted line indicates the horizontal domain of Geo-CAPE airborne simulator (GCAS) measurements taken during the GMAP-2021 campaign.

816

817



818



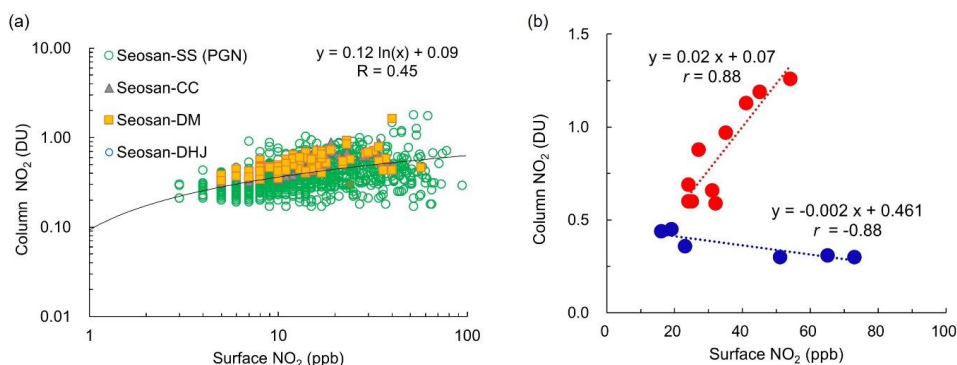
819

820 **Figure 2.** Flight tracks for two Cessna Grand Caravan 208 B aircraft over Pandora sites (left)  
 821 PA<sub>4</sub> and (right) PA<sub>1</sub> during the GMAP-2020 campaign. Colored circles indicate airborne NO<sub>2</sub>  
 822 concentration observations. Stacked circles indicate spiral flights conducted over two sites.

823

824

825



826

827 **Figure 3.** a) Pandora column (PC) NO<sub>2</sub> measurements as a function of surface *in situ* (SI) NO<sub>2</sub>  
 828 observations at Pandora sites PA<sub>1</sub>–PA<sub>3</sub> during the GMAP-2020 campaign and PA<sub>4</sub> during a 1-  
 829 year period. A logarithmic regression model was used to evaluate the relationship between PC  
 830 and SI measurements (black line). (b) Sample scatter plots of PC-NO<sub>2</sub> and SI-NO<sub>2</sub> for February  
 831 24 (red) and April 21 (blue), 2021.



832

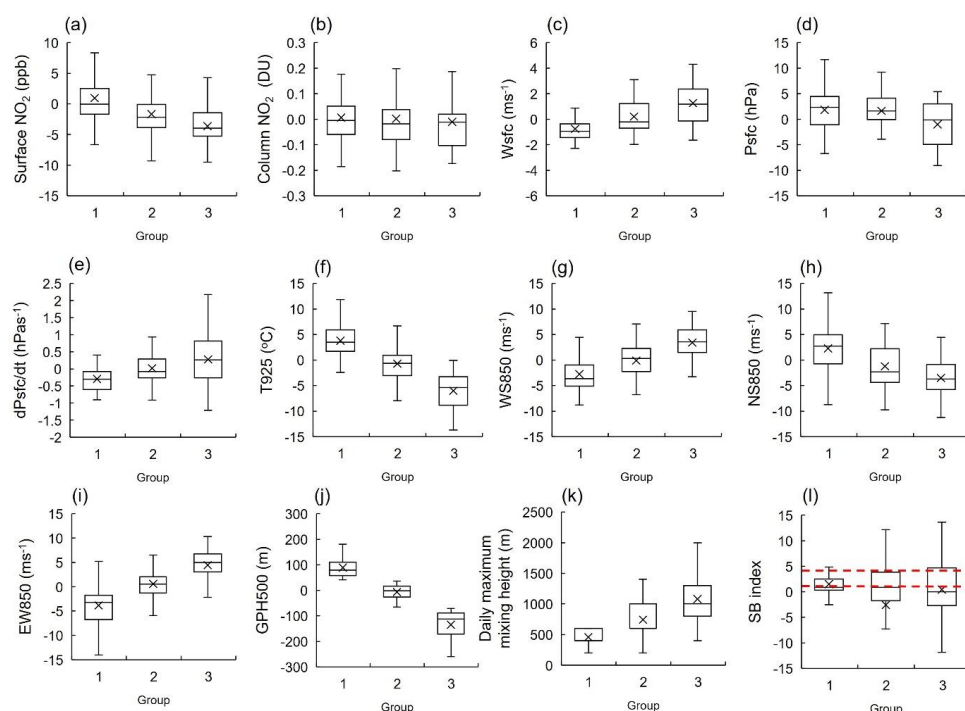


**Figure 4.** K-means clustering yielded three groups of cases for (a) surface  $\text{NO}_2$  and (b) PC- $\text{NO}_2$ , associated with eight meteorological variables: (c) surface wind speed ( $W_{\text{sfc}}$ ), (d)  $P_{\text{sfc}}$ , (e)  $P_{\text{sfc}}$  tendency ( $dP_{\text{sfc}}/dt$ ), (f) 925-hPa air temperature ( $T_{925}$ ), (g) 850-hPa wind speed ( $W_{850}$ ), (h) 850-hPa north-south wind component ( $NS_{850}$ ), (i) 850-hPa east-west wind component ( $EW_{850}$ ), and (j) 500-hPa geopotential height ( $GPH_{500}$ ). All data were de-seasonalized using the 30-day moving average, except PC- $\text{NO}_2$ , for which the monthly average was used. (k) Simulated daily maximum mixing height (not directly clustered). (l) Box and whisker plots of the sea breeze index (SBI) at Seosan for the 1-year period. Red dots indicate critical SBI values (3: Biggs and Graves, 1962).

842

843

844

845

846

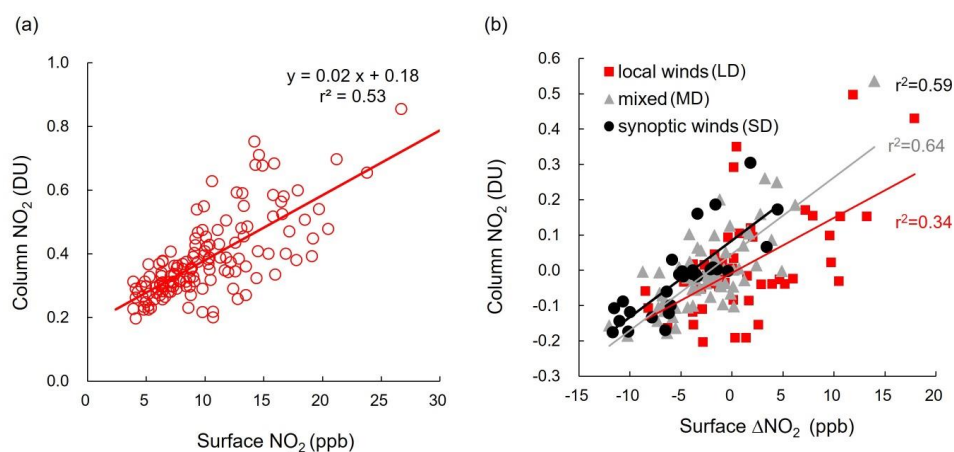


**Figure 5.** Scatter plots of daytime mean PC-NO<sub>2</sub> vs. SI-NO<sub>2</sub> measurements at site PA<sub>4</sub> under (a) all meteorological conditions and (b) each meteorological condition over a period of 1 year (November 12, 2020–October 30, 2021).

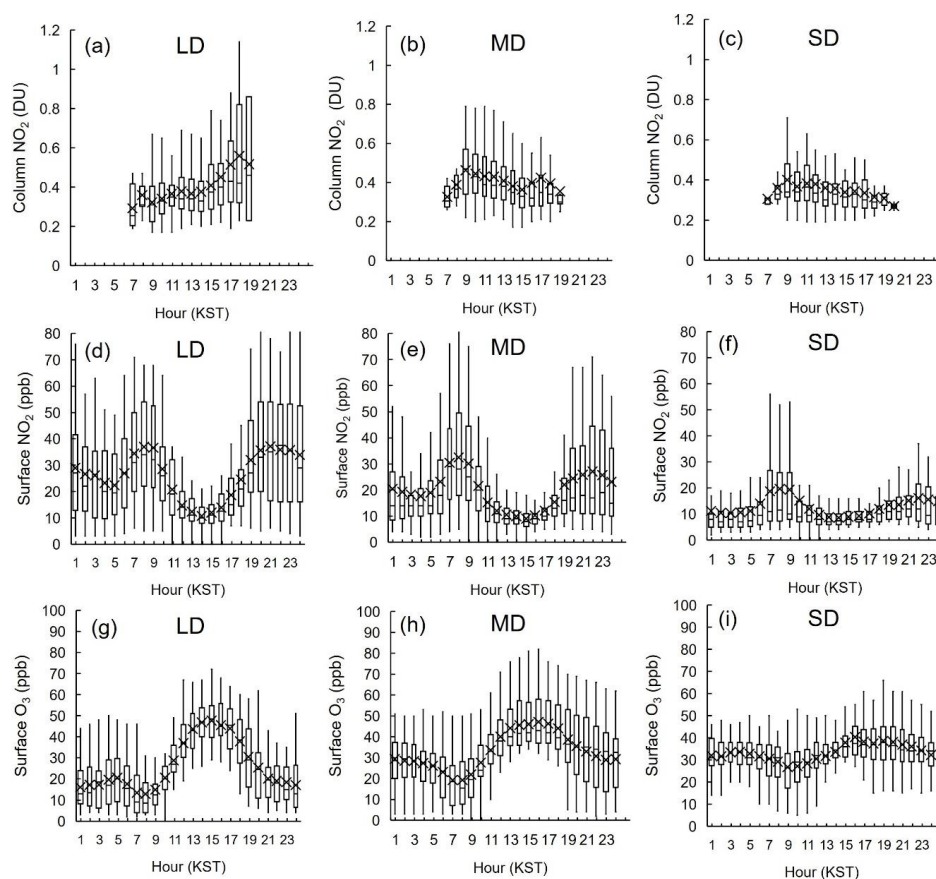
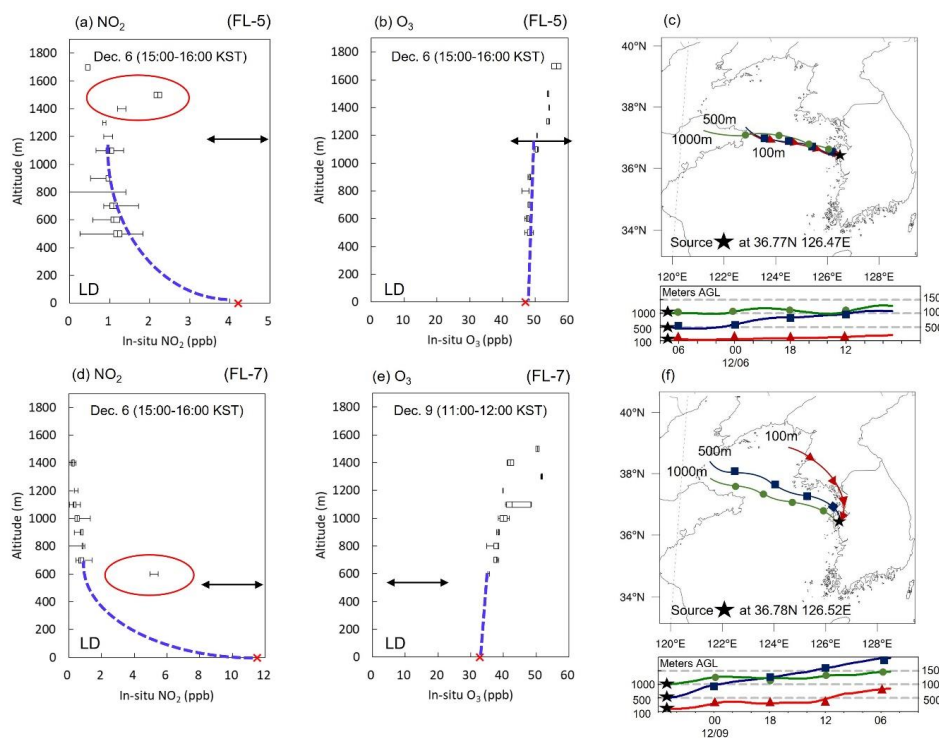


**Figure 6.** Box and whisker plots of diurnal variations in (a–c) PC- $\text{NO}_2$ , (d–f) SI- $\text{NO}_2$ , and (g–i) surface  $\text{O}_3$  under synoptic wind-dominant (SD), mixed (MD), and local wind-dominant (LD) conditions in Seosan during a 1-year period (November 12, 2020–October 30, 2021).



881

882



883

884 **Figure 7.** Box and whisker plots of the vertical  $\text{NO}_2$  and  $\text{O}_3$  profiles measured by GMAP  
 885 aircraft superposed with *in situ* AQMS<sub>1</sub> measurements during flights (a, b) FL-1 (November  
 886 26) and (d, e) FL-8 (December 12). Blue dashed lines are linear regression lines fitted to  $\text{NO}_2$   
 887 and  $\text{O}_3$  profiles within the planetary boundary layer (PBL). Black arrows indicate the simulated  
 888 PBL height (PBLH) obtained from the Korea Meteorological Administration (KMA).  
 889 HSYPLIT 24-h backward trajectories in Seosan are shown at altitudes of 100, 500, and 1,000  
 890 m, starting at 1600 KST on November 26 and 1200 KST on December 12.

891

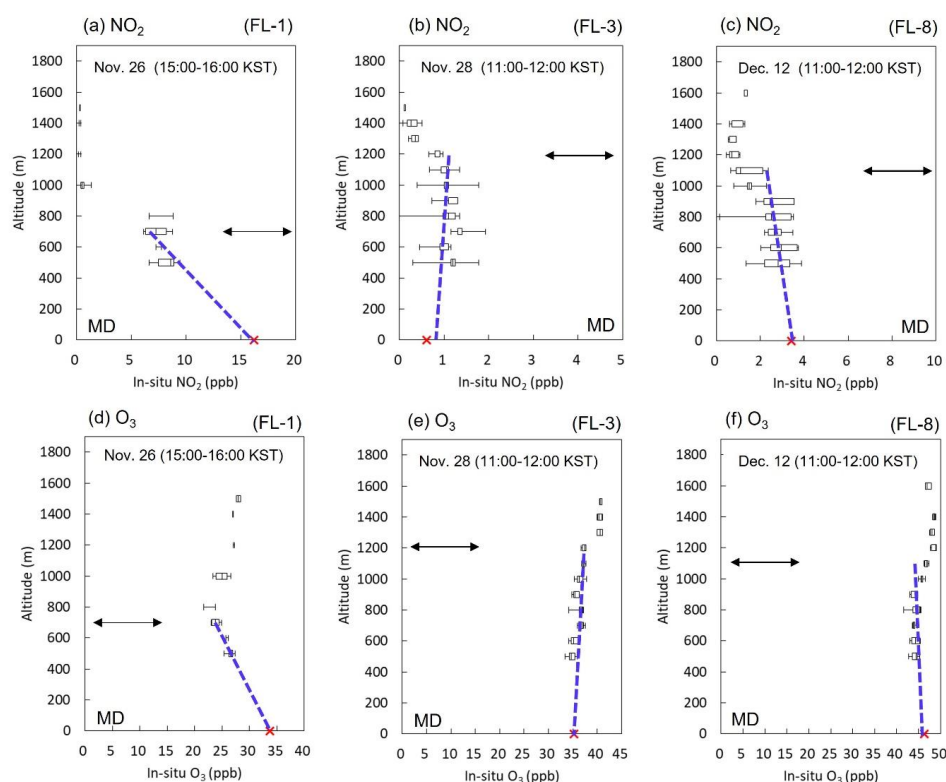
892

893

894



895



896

897 **Figure 8.** Box and whisker plots of vertical profiles obtained from GMAP aircraft superposed  
 898 with *in situ* AQMS measurements for (1) NO<sub>2</sub> and (2) O<sub>3</sub> for flights (a) FL-1 (November 26),  
 899 (b) FL-3 (November 28), and (c) FL-8 (December 12). Blue dashed lines are linear regression  
 900 lines fitted to NO<sub>2</sub> and O<sub>3</sub> in the PBL. Black arrows indicate PBLH simulated by the Hybrid  
 901 Single-Particle Lagrangian Integrated Trajectory (HYSPLIT) Global Forecast System (GFS).

902

903

904

905

906

907



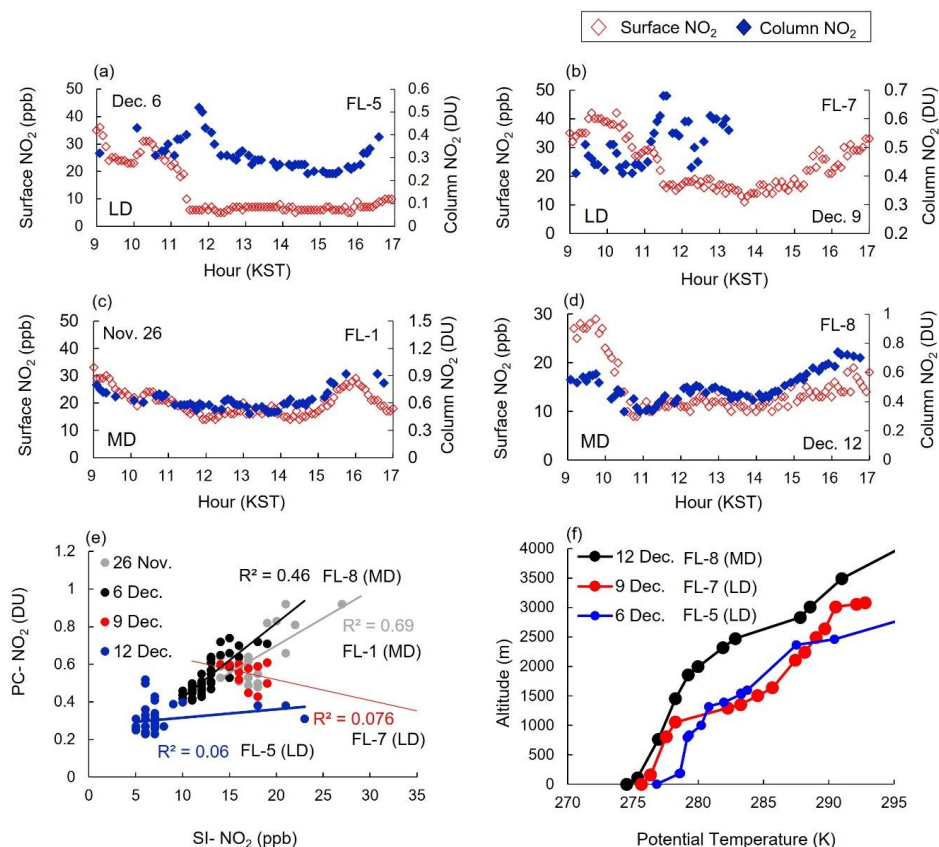
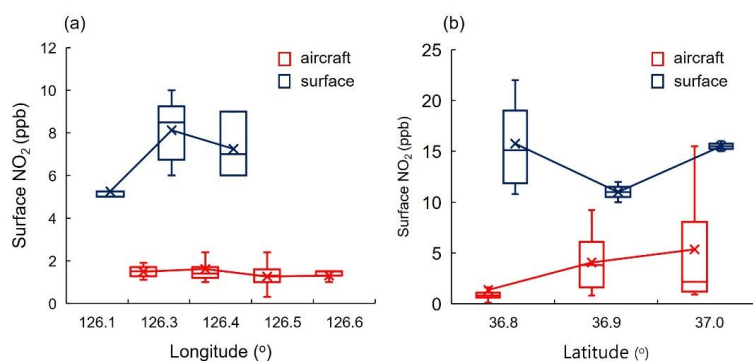


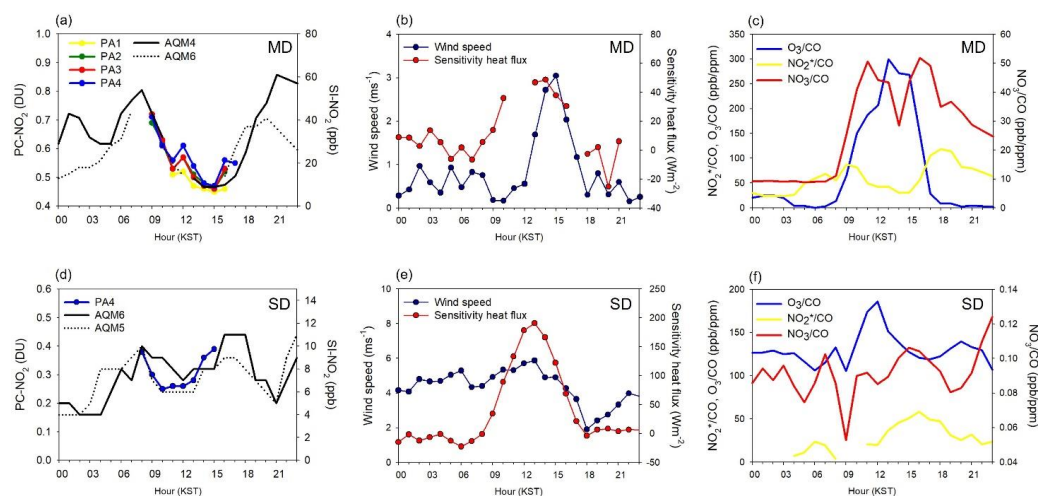
**Figure 9.** Time series and scatter plots of PC-NO<sub>2</sub> and SI-NO<sub>2</sub> at PA<sub>2</sub> on (a) December 6, (b) December 9, (c) November 26, and (d) December 12. (e) Scatter plot of PC-NO<sub>2</sub> and SI-NO<sub>2</sub> on December 6 (blue), December 9 (red), November 26 (gray), and December 12 (black). (f) Vertical potential temperature profiles on December 6, 9, and 12, 2020. Radiosonde data for November 26, 2020 are missing.



920

921 **Figure 10.** Latitudinal NO<sub>2</sub> distribution at the surface and 600 m over PA<sub>4</sub> (Seosan Super Site),  
 922 averaged during (a) 1300–1600 KST on December 6 (FL-5) by longitude and (b) 1200–1400  
 923 KST on December 9 (FL-7) by latitude, obtained from airborne (blue) and surface  
 924 measurements (red).

925



926

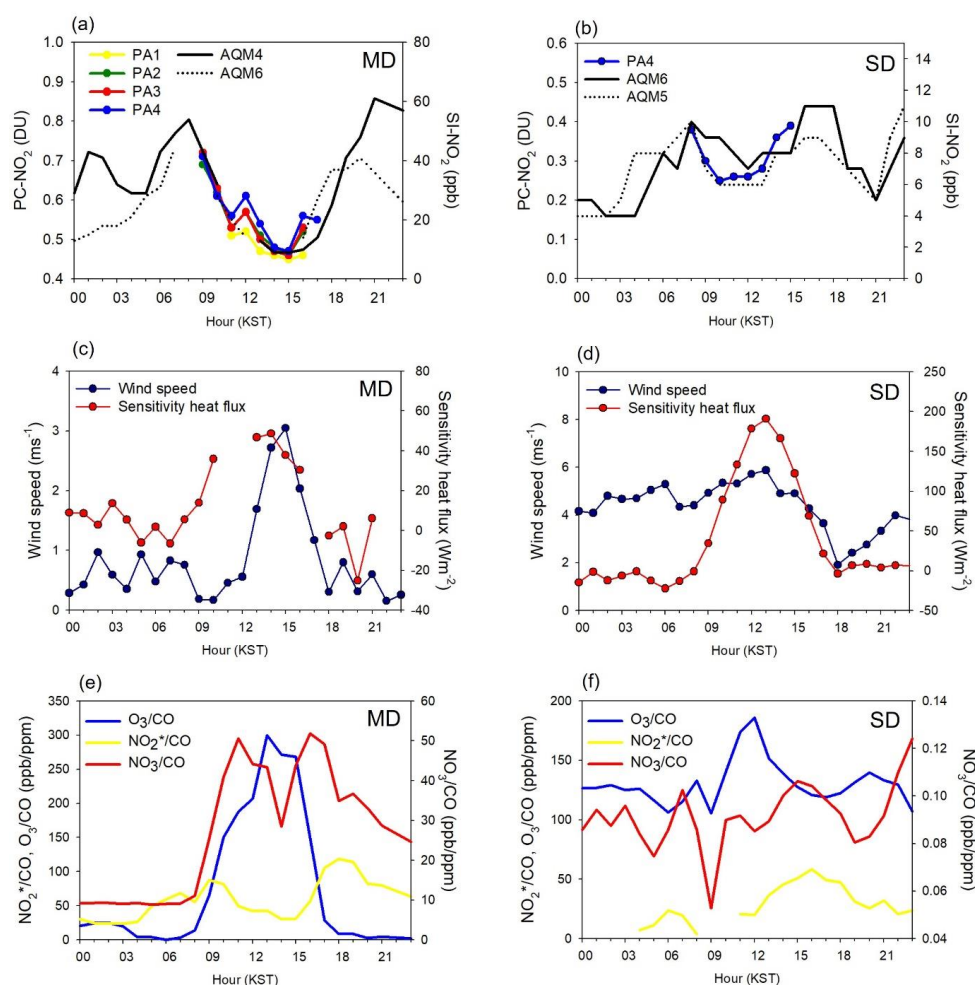


**Figure 11.** Example of diurnal variations on November 25 (a, c) and December 14 (d, f). (a, d) Column  $\text{NO}_2$  at sites PA<sub>1</sub>–PA<sub>4</sub> and surface  $\text{NO}_2$  at the air quality monitoring sites AQM<sub>4</sub> and AQM<sub>6</sub>. (b, e) Sensible heat fluxes and surface wind speed at PA<sub>4</sub>. (c, f) Diurnal variations in  $\text{NO}_2$ ,  $\text{NO}_2^+$ , and  $\text{O}_3$  normalized by CO. A map of the measurement sites is shown in Figure 1.